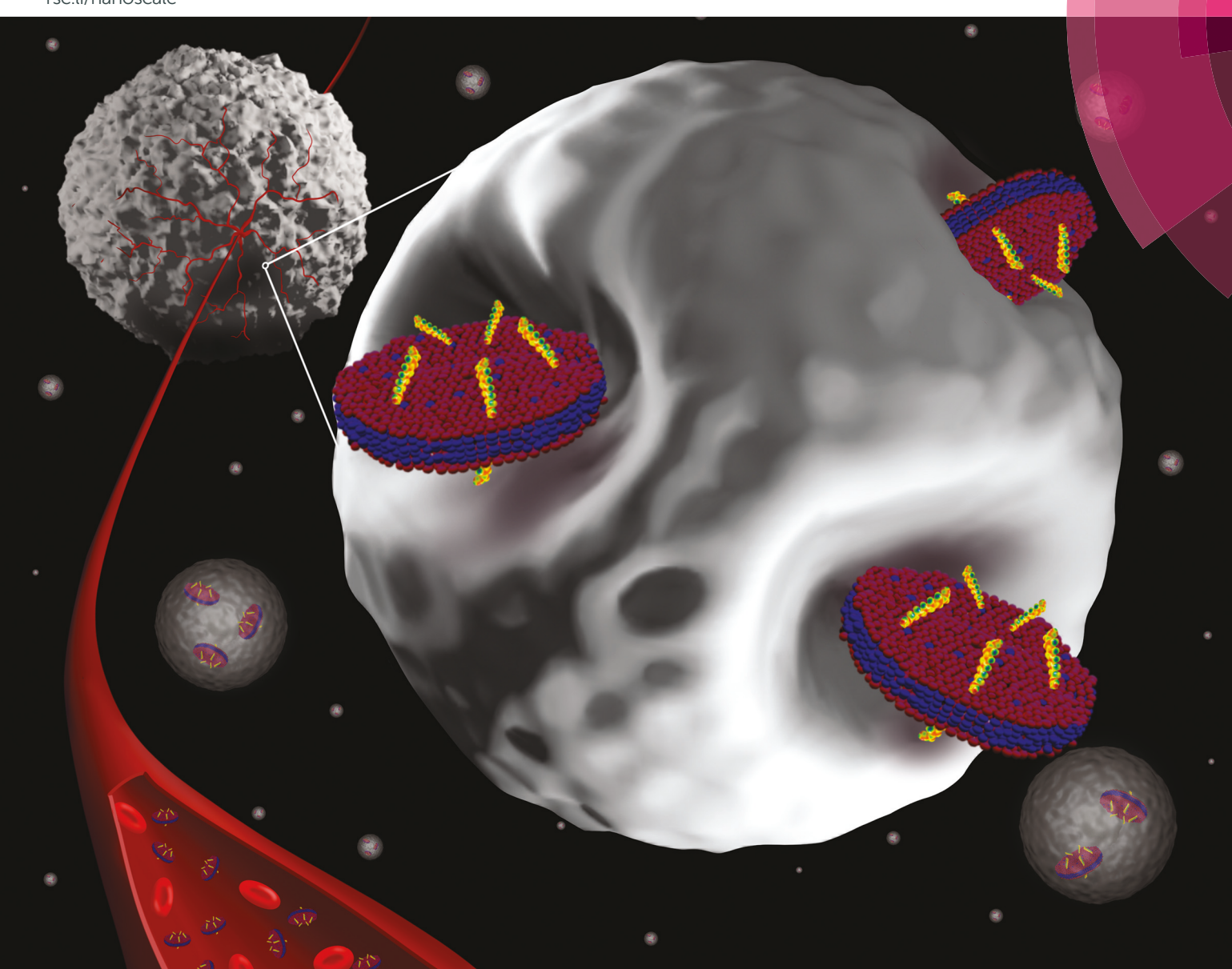
# Nanoscale

rsc.li/nanoscale



ISSN 2040-3372



#### PAPER



# **Nanoscale**



# **PAPER**



Cite this: Nanoscale, 2019, 11, 12517

# A universal discoidal nanoplatform for the intracellular delivery of PNAs†

Armin Tahmasbi Rad, ‡<sup>a,b</sup> Shipra Malik, ‡<sup>c</sup> Lin Yang, <sup>d</sup> Tripat Kaur Oberoi-Khanuja, <sup>e</sup> Mu-Ping Nieh and Raman Bahal k<sup>c</sup>

Peptide nucleic acids (PNAs) have gained considerable attention due to their remarkable potential in gene editing and targeting-based strategies. However, cellular delivery of PNAs remains a challenge in developing their broader therapeutic applications. Here, we investigated a novel complex made of lipid bicelles and PNA-based carriers for the efficient delivery of PNAs. For proof of concept, PNAs targeting microRNA (miR) 210 and 155 were tested. Comprehensive evaluation of positive as well as negative charge-containing bicelles with PNA: lipid ratios of 1:100, 1:1000, and 1:2500 was performed. The negatively charged bicelles with a PNA: lipid molar ratio of 1:2500 yielded a discoidal shape with a uniform diameter of ~30 nm and a bilayer thickness of 5 nm, while the positively charged bicellar system contained irregular vesicles after the incorporation of PNA. Small-angle X-ray scattering (SAXS) analysis was performed to provide insight into how the hydrophobic PNAs interact with bicelles. Further, flow cytometry followed by confocal microscopy analyses substantiate the superior transfection efficiency of bicelles containing dyeconjugated antimiR PNAs. Functional analysis also confirmed miR inhibition by PNA oligomers delivered by bicelles. The nanodiscoidal complex opens a new pathway to deliver PNAs, which, on their own, are a great challenge to be endocytosed into cells.

Received 29th April 2019, Accepted 23rd May 2019 DOI: 10.1039/c9nr03667a

rsc.li/nanoscale

## 1. Introduction

The use of peptide nucleic acids (PNAs) has expanded widely in the last few years, not only for their role in basic research but also in therapeutic areas pertaining to gene editing and targeting. PNAs are artificial DNA mimics that consist of pyrimidine or purine nucleobases attached to a highly flexible pseudopeptide backbone. It has been well established that PNAs bind with high affinity to genomic DNA and RNA targets based on Watson–Crick recognition principles and thus regulate gene expression. In addition, the neutral backbone of PNAs confers it resistance to enzymatic degradation.

Several promising chemical, mechanical, and electrical transduction-based methods have been explored for increasing the intracellular delivery of PNAs.<sup>6-8</sup> However, these methods can only apply to small experimental conditions and cannot translate to in vivo studies or clinical applications. Additionally, transduction reagents often lead to off-target and cytotoxic effects. Similarly, a series of cationic residues conjugated to PNAs have been explored that could aid the cellular uptake of PNAs by increasing their degree of interaction with the negatively charged cell membrane.9 Though these strategies have shown promise up to a certain extent, the inclusion of cationic groups also increases cytotoxicity both in vitro as well as in vivo. Other possibilities for incorporating the transduction domain onto the achiral backbone of PNAs have been investigated. These include the development of guanidiniumand lysine-based chemically modified gamma PNAs. 10,11 However, these methods require complicated synthetic procedures and elaborate optimization to generate ample material, especially for in vivo studies.

Recently, nanoparticle (NP)-based strategies have garnered attention for delivering PNAs in fundamental as well as bio-

aforementioned unique properties of PNAs make it an attractive reagent for therapeutic and diagnostic applications. However, intracellular delivery, *i.e.*, how to get PNAs across the lipid-bilayer cell membrane, always presents an enormous challenge and prevents their broader application.<sup>5</sup>

<sup>&</sup>lt;sup>a</sup>Department of Biomedical Engineering, University of Connecticut, Storrs, CT, 06269, USA. E-mail: Mu-Ping.Nieh@UConn.edu

<sup>&</sup>lt;sup>b</sup>Polymer Program, Institute of Materials Sciences, University of Connecticut, 191 Auditorium Road, Storrs, CT 06269, USA

<sup>&</sup>lt;sup>c</sup>School of Pharmacy, University of Connecticut, Storrs, CT, 06269, USA. E-mail: Raman.Bahal@UConn.edu

<sup>&</sup>lt;sup>d</sup>National Synchrotron Light Source – II, Brookhaven National Laboratory, Upton,

<sup>&</sup>lt;sup>e</sup>Department of Dermatology, University of California, San Francisco, CA, USA <sup>f</sup>Department of Chemical and Biomolecular Engineering, University of Connecticut, Storrs, CT, 06269, USA

<sup>†</sup>Electronic supplementary information (ESI) available. See DOI: 10.1039/c9nr03667a

<sup>‡</sup>These authors contributed equally to this work.

medical research. Several NPs, such as avidin, <sup>12</sup> zeolites, <sup>13</sup> mesoporous silica, <sup>14</sup> and cationic shell cross-linked knedellike NPs, <sup>15</sup> just to name a few, have been reported to deliver PNAs. Moreover, the use of the FDA-approved poly-lactic-*co*-glycolic acid (PLGA)-based NPs to deliver PNAs has also been tested extensively. <sup>6,16,17</sup> Though these PLGA-based NPs have shown promise to some extent, their synthesis does not yield NPs containing the high payload of PNAs that is necessary for clinical efficacy.

Recently, a low-polydispersity, spontaneously forming discoidal bicelle or nanodisc (ND) with a diameter of ~30 nm and a thickness of 5 nm, comprised by a mixture of longand short-chain lipids, has been employed for entrapping hydrophobic molecules with a robust formation/assembly mechanism. 18,19 The membrane-mimicking bicelles can be stabilized by polyethylene glycol-conjugated (PEGylated) lipids and easily incorporated with amphiphilic biomolecules such as membrane proteins, making them an attractive system for solubilization, isolation, and purification, as well as for use in the biophysical and biochemical studies of membrane proteins. 20,21 Our prior study indicated that the cellular uptake of bicelles is  $\sim$ 5–10 times greater than that of spherical vesicles with identical chemical composition, because they take more routes of internalization than the vesicles do. 22,23 Enhanced uptake, more diverse mechanisms for endocytosis, and faster diffusion across the membranes due to their small size<sup>24</sup> make bicelles a better candidate than the conventional polymeric and inorganic spherical nanocarriers. 25-28,29

In this study, several bicelle-PNA nanocomplexes were characterized in structure and designed for optimal endocytotic delivery. The new class of nanocarriers shows excellent transfection efficiency with low toxicity and high payload. Here, we utilized NDs for the delivery of antimiRs targeting miR-155 (PNA-155) and 210 (PNA-210). We performed comprehensive evaluation of loading capacity, size, morphology, and efficacy of antimiR-155 and 210 PNA-containing bicelles. Additionally, we performed molecular modeling and small-angle X-ray scattering (SAXS) to evaluate the interaction of hydrophobic PNAs with lipids. We further analyzed the transfection efficiencies of these NDs in cervical cancer cells (HeLa) and comprehensively evaluated the cellular uptake mechanism of bicelles containing antimiR PNAs in HeLa cells. Our results highlight the efficient and safe bicelle-mediated delivery of PNAs that can be used effectively for extensive biomedical applications.

#### 2. Materials and methods

#### 2.1 Materials

The zwitterionic short-chain dihexanoyl phosphatidylcholine (di-6:0, DHPC) lipid, the zwitterionic long-chain dipalmitoyl phosphatidylcholine (di-16:0, DPPC) lipid, the negatively charged long-chain dipalmitoyl phosphatidylglycerol (DPPG), 1,2-dipalmitoyl-3-trimethylammonium-propane (chloride salt; DOTAP), and polyethylene glycol (PEG2000)-conjugated distearoyl phosphoethanolamine (DSPE-PEG2000) were purchased from Avanti

Polar Lipids (Alabaster, AL, USA). They were used without further purification. Phosphate-buffered saline (PBS) powder was purchased from Sigma-Aldrich (St Louis, MO). Dulbecco's phosphate-buffered saline (DPBS) was purchased from Life Technologies (Grand Island, NY, USA). Boc-protected PNA monomers used for PNA synthesis were purchased from ASM Chemicals and Research (Hanover, Germany). Boc-MiniPEG and N $\alpha$ -t-butyloxycarbonyl-N $\gamma$ -benzyloxycarbonyl-L-lysine (Boc-Lys(Z)-OH) were purchased from Peptides International (Kentucky, USA). Boc-5-carboxytetramethylrhodamine (TAMRA) dye was purchased from VWR (Radnor, Pennsylvania).

Chlorpromazine, amiloride, and genistein were purchased from Sigma-Aldrich (MO, USA). Human embryonic kidney (HEK) cells (ATCC® CRL-1573<sup>TM</sup>) were purchased from ATCC (Virginia, USA). CellTiter 96® Aqueous One Solution Cell Proliferation Assay (MTS) was purchased from Promega (WI, USA).

#### 2.2 Synthesis of lipid NPs of different shapes

DPPC, DHPC, and DSPE-PEG2000, as well as either negatively charged DPPG or positively charged DOTAP were used to prepare NPs. The mixture DPPC/DHPC/DPPG/DSPE-PEG2000 was prepared at a molar ratio of 69.58/25.1/3.76/2.0.<sup>23</sup> All lipid molecules of the required weights were first homogenized in chloroform. After removal of the solvent by a vacuum oven, the dried samples were then re-dispersed in filtered deionized (DI) water to make stock suspensions with a total lipid weight concentration,  $C_{\rm lp}$ , of 10% (wt). After successive vortex and temperature cycling between 25 °C and 70 °C, the stock dispersions were progressively diluted at room temperature to  $C_{\rm lp}$  = 1.0 mg ml<sup>-1</sup> with PBS solution.

The PNA-entrapped bicelles were prepared at PNA:lipid molar ratios of 1:200, 1:500, 1:1000 and 1:2500, homogeneously dispersed in chloroform. After being dried, the sample was re-hydrated in water to form a 10 wt% mother solution by proper temperature cycling and vortexing. The solution was then centrifuged at 10 000 rpm for 10 minutes in a Beckman Coulter centrifuge to separate the aggregates and large particles, and diluted to the desired concentration prior to use. The highest achievable concentration for encapsulated PNA is on the basis of 10 wt% lipid concentration.

#### 2.3 Measuring the loading of antimiRs in NDs

In order to investigate the encapsulation efficiencies of the PNAs, aqueous solutions of the bicelle-encapsulated PNAs were diluted to 0.1 wt% lipid concentration and centrifuged at 10 000 rpm for 15 minutes. The top supernatant was separated as the encapsulated portion. The precipitates also were used to confirm the amount of non-encapsulated PNAs. Both supernatants and precipitates were dried under nitrogen gas and redispersed accordingly with DMSO. After separating the precipitate and supernatant, the UV-visible absorption spectra (190–800 nm) of all samples were recorded by a Cary 5000 UV-Vis-NIR spectrometer (Agilent, USA). The absorbance measurements of lipid compositions and PNA molecules alone were also used for the pre-calibrated curves and extinction coefficient confirmation. The encapsulation efficiency (EE) of

encapsulated PNAs in each sample was measured via the equation below:

$$EE = \frac{[(OD \times M_w \times dilution factor)/\varepsilon]}{Initial Concentration} \times 100,$$

where OD,  $M_{\rm w}$ , and  $\varepsilon$  are the optical density (normalized absorbance intensity), molecular weight of the PNA, and extinction coefficient, respectively; the dilution factor is 1000, and the initial concentration is 0.01 wt% of lipid nanocarrier.

#### 2.4 Small-angle X-ray scattering (SAXS)

SAXS measurements were conducted using the 16ID-LiX Beamline at the National Synchrotron Light Source II, located at the Brookhaven National Laboratory (Upton, NY), with the standard flow-cell-based solution scattering setup and the X-ray energy of 13.5 keV. SAXS intensity is expressed as a function of the scattering vector, q ( $q = \frac{4\pi}{\lambda} \sin \frac{\theta}{2}$ , where  $\theta$  is the scattering angle), which varies from 0.005 to 2.5 Å<sup>-1</sup>. <sup>30</sup> Radial averaging and q-conversion of data were performed using the standard software, <sup>31</sup> merging data from all three detectors used in the measurements. Transmission correction and background subtraction were performed to minimize the intensity of the hydrogen bond from water at ~2.0 Å<sup>-1</sup>.

#### 2.5 Dynamic light scattering (DLS)

Size and population distribution of pristine and encapsulated PNA nanodiscs were also determined using an ALV/CGS-8F/4 instrument (ALV compact system, Germany) with a  $\lambda$  = 632.8 nm laser beam. The samples were dissolved and homogenized in filtered DI water to 0.1 wt%. The results were reported as the average of 10 measurements.

#### 2.6 Transmission electron microscopy (TEM)

Negatively stained transmission electron microscopy (TEM) images were obtained using FEI Tecnai T12. The samples were prepared by spreading 5  $\mu L$  of 0.001 wt% solution on a 400 mesh Formvar/carbon film copper grid (Electron Microscopy Sciences, PA, USA), and negative staining was applied with 10 mg mL $^{-1}$  of uranyl acetate (SPI Supplies, PA, USA). The grids were then dried at 25 °C. The accelerating voltage of the TEM was set at 80 kV.

#### 2.7 Atomic force microscopy (AFM) analysis

A 0.01 wt% solution of the ND (–) PNA-155 1:2500 was freshly made, then placed on a freshly cleaved mica surface and dried. Soft silicon nitride cantilevers (Bruker Nano, Camarillo, CA) with silicon nitride tips were used, with a nominal tip radius of 2 nm. Experiments were performed at room temperature using an MFP-3D-BIO AFM (Asylum Research, Santa Barbara, CA) in contact mode with a scanning rate of 0.7 Hz.

#### 2.8 Calculation of molecular lipophilic surface potential (MLSP)

MLSP describes the 3-D lipophilic influence of all fragments of a molecule<sup>32</sup> and can be calculated at given points in space.<sup>33</sup> MLSP analysis of the PNA 155-TAMRA and PNA 210-TAMRA

molecules was carried out using the Molinspiration Property Calculation Service molecular modeling package in order to study the feasibility of encapsulation inside the lipid bilayers of nanodiscs.<sup>34</sup> Gasteiger–Hückel charges were assigned to the atoms of the TMS structure, and surfaces were generated. The color ramp for the MLSP ranges from violet/blue, representing higher lipophilic potential (LP), to red, representing lower LP.

#### 2.9 AntimiR-PNA based oligomers

PNA-155 and PNA-210 were synthesized via solid-phase synthesis using MBHA (4-methylbenzhydrylamine) resin and Bocmonomers (A, T, C, G).35 TAMRA dve was conjugated to the N-terminus of PNAs with a Boc-miniPEG-3 linker (OOO). PNAs were then cleaved from the resin using a cleavage cocktail containing m-cresol: thioanisole: trifluoromethanesulfonic acid (TFMSA): trifluoroacetic acid (TFA) (1:1:2:4) followed by precipitation using diethyl ether. PNAs were purified and characterized using reverse-phase high-performance liquid chromatography (HPLC) and matrix-assisted laser desorption/ionization-time of flight (MALDI-TOF) spectroscopy, respectively. The concentration of PNAs was determined using UV-vis spectroscopy, and the extinction coefficient of PNAs was calculated using the extinction coefficients of individual monomers  $[13700 \text{ M}^{-1} \text{ cm}^{-1} \text{ (A)}, 6600 \text{ M}^{-1} \text{ cm}^{-1} \text{ (C)}, 11700 \text{ M}^{-1} \text{ cm}^{-1}]$ (G), and  $8600 \text{ M}^{-1} \text{ cm}^{-1}$  (T)] of the sequence.

PNA sequences used in the study are as follows:

PNA-155-TAMRA: 5'-TAMRA-000-ACCCCTATCACGATTAGCATTAA-Lys-3'

PNA-210-TAMRA: 5'-TAMRA-000-TCAGCCGCTGTCACACGC-ACAG-Lys-3'.

#### 2.10 Confocal microscopy

Approximately 100 000 HeLa cells (ATCC® CCL-2TM) were allowed to seed overnight on coverslips in 12-well plates. Cells were treated with only PNA-155-TAMRA, and PNA-155-TAMRA or PNA-210-TAMRA entrapped in optimized NDs [1:2500(-)] overnight. The amount of PNA-155-TAMRA used was kept at the same level as that entrapped in nanodiscs. After 24 hours, the cells were gently washed with 1 mL phosphate-buffered saline (PBS, 4×) at room temperature (RT). Further, the cells were fixed by adding 1 mL of 4% paraformaldehyde at 37 °C for 10 minutes. After washing the cells with 1 mL PBS (2×), cells were permeabilized using 1 mL of 0.1% Triton-X in PBS at 37 °C for 10 minutes. Cells were mounted on a slide using ProLong<sup>TM</sup> Diamond Antifade Mountant with DAPI (Life Technologies, Carlsbad, CA, USA). Samples were allowed to harden at 4 °C overnight, and images were taken using a Nikon A1R spectral confocal microscope.

#### 2.11 Flow cytometry analysis

Approximately 100 000 HeLa cells (ATCC® CCL- $2^{TM}$ ) were seeded in 12-well plates overnight, followed by treatment with PNA-210-TAMRA- or PNA-155-TAMRA-containing NDs for 24 hours. Cells were then washed with PBS (4×), and trypsinization was done using 0.25% trypsin-EDTA (Gibco®, Life Technologies) at 37 °C for 4 minutes. Trypsinized cells were

suspended in 1 mL of DMEM with 10% FBS and centrifuged at 1000 RPM for 4 minutes at 4 °C. Further, the cells were washed twice with 1 mL of PBS at 1000 RPM for 4 minutes at 4 °C. Fixation of cells was done using 300  $\mu L$  of 4% paraformaldehyde, and flow cytometry was done using the LSR Fortessa X-20 Cell Analyzer (BD Biosciences, San Jose, CA). Results obtained were analyzed using the FlowJo analysis software.

#### 2.12 Real-time PCR studies

RNA was extracted from HeLa cells (ATCC® CCL-2<sup>TM</sup>) treated with PNA-155-TAMRA and nanodiscs containing PNA-155-TAMRA using the RNeasy Mini Kit (Qiagen, Hilden, Germany). TaqMan<sup>TM</sup> MicroRNA Assay (Assay ID: 467534\_mat; Applied Biosystems, Foster City, CA) was used to measure miR-155 levels. cDNA was synthesized using miR-155 reverse transcriptase (RT) primers (TaqMan<sup>TM</sup> MicroRNA Assay), 10× RT buffer, and 100 mM dNTPs in the presence of RNase inhibitor (Applied Biosystems, Foster City, CA). Reverse transcription was done under the specified conditions (16 °C for 30 minutes, 42 °C for 30 minutes, 85 °C for 5 minutes) provided with the TaqMan<sup>TM</sup> MicroRNA Assay using the thermal cycler (T100<sup>TM</sup>, Bio-Rad, Hercules, CA).

MiR-155-specific primers (TaqMan<sup>TM</sup> MicroRNA Assay) and TaqMan<sup>TM</sup> Universal Master Mix II with UNG (Applied Biosystems, Foster City, CA) were used under the conditions specified in the assay [50 °C for 2 minutes, 95 °C for 10 minutes, (95 °C for 15 seconds, 60 °C for 60 seconds)  $\times$  40 cycles] for amplification of cDNA. U6 snRNA (TaqMan<sup>TM</sup> microRNA control) assay was used as a control. No template control was used for both the U6 snRNA and miR-155 expression levels.

#### 2.13 Endocytosis inhibitor study

HeLa cells were incubated with chlorpromazine (10  $\mu g$  mL<sup>-1</sup>), amiloride (10 mM) and genistein (200  $\mu$ mol l<sup>-1</sup>) at 37 °C. After 30 minutes, cells were treated with PNA-155-TAMRA bicelles at a dose of 4  $\mu$ M ml<sup>-1</sup> for one hour at 37 °C. Further, cells were washed with PBS and fixed using 4% paraformaldehyde, followed with analysis using the LSR Fortessa X-20 Cell Analyzer (BD Biosciences, San Jose, CA). For confocal microscopy, cells were pretreated with endocytosis inhibitors for 30 minutes, then incubated with PNA-155-TAMRA bicelles for one hour. After washing and fixing with 4% paraformaldehyde, cells were mounted in ProLong<sup>TM</sup> Diamond Antifade Mountant with DAPI (Life Technologies, Carlsbad, CA, USA). Images were taken using a Nikon A1R spectral confocal microscope.

#### 2.14 Safety study in primary cells

Human embryonic kidney (HEK) 293 cells (2000 cells per well) were seeded overnight in 96-well plates. Cells were treated with PNA-155-TAMRA bicelles in varying amounts (1  $\mu$ M ml<sup>-1</sup>, 2  $\mu$ M ml<sup>-1</sup>, 4  $\mu$ M ml<sup>-1</sup>, 6  $\mu$ M ml<sup>-1</sup>, and 8  $\mu$ M ml<sup>-1</sup>) and incubated at 37 °C. After 24 hours, cells were washed with PBS and incubated in fresh culture medium with 20  $\mu$ l of MTS reagent (CellTiter 96® Aqueous One Solution Cell Proliferation Assay)

at 37 °C. After an hour, absorbance was measured at 490 nm and used to calculate percent cell viability.

#### 2.15 Western blot analysis

HeLa cells were treated with NDs, and protein was extracted with a radio-immunoprecipitation assay lysis buffer. Total protein of 50–100  $\mu g$  was run on SDS/polyacrylamide electrophoresis gels and transferred to nitrocellulose membranes. Antibodies used are as follows: anti-p53 antibody (DO-1; SCBT – Santa Cruz Biotechnology, sc-126) at 1:500 and anti-β-actin antibody (Sigma, A5316) at 1:10 000.

## 3. Results

To assess whether the sequences of PNAs will affect their encapsulation and characteristics in bicelles, we developed and optimized the delivery systems for two potential antimiRs: PNA-210 and 155, targeting miR-210 and 155, respectively. miR-210 is upregulated in almost all solid tumors, including breast, cervical, pancreatic, and colorectal cancer. Similarly, miR-155 is upregulated in lymphoma as well as leukemia. Tambe We tested PNA-carboxytetramethylrhodamine (TAMRA) conjugates that can be used for both imaging and efficacy studies.

#### 3.1 Lipid-based bicellar formulations

First, we formulated positively and negatively charged bicelles (or NDs) to evaluate their antimiR-PNA payload properties. In parallel, we compared three formulations comprising different PNA: lipid molar ratios of 1:2500, 1:1000, and 1:200. NDs were formulated based on the established protocol. We did not notice any significant decrease in reaction yield in the formulation process of NDs containing antimiR PNAs.

#### 3.2 ND characterization

We measured the distribution of the hydrodynamic radii  $(R_H)$ of antimiR-loaded and pristine bicelles using a dynamic light scattering (DLS) method. In the pristine NDs, a radius of ~8.5 nm was observed that is consistent with the literature.  $^{21,23}$  However, we noticed an increase in  $R_{\rm H}$  for antimiR PNA-loaded negatively charged bicelles regardless of their surface charge (Fig. 1A). For the samples with PNA: lipid molar ratios of 1:2500 and 1:1000, the  $R_{\rm H}s$  remain less than ~15 nm with a uniform distribution (Fig. S1†), while as the PNA: lipid molar ratio reaches 1:100, the R<sub>H</sub> increases significantly with a broader distribution, indicative of PNA-induced irregularity. Further, our results showed similar size and uniformity for both PNAs, i.e., antimiR PNA-155 and PNA-210, at corresponding compositions, implying that the negatively charged bicelle is capable of encapsulating the antimiR regardless of their nucleobase sequence composition. In contrast to the negatively charged bicelles, the positively charged bicelles result in large aggregates even at PNA: lipid ratios of 1:1000 and 1:2500, making them unlikely to fully retain the nanodiscoidal shape. Apparently, the electrostatic interaction between

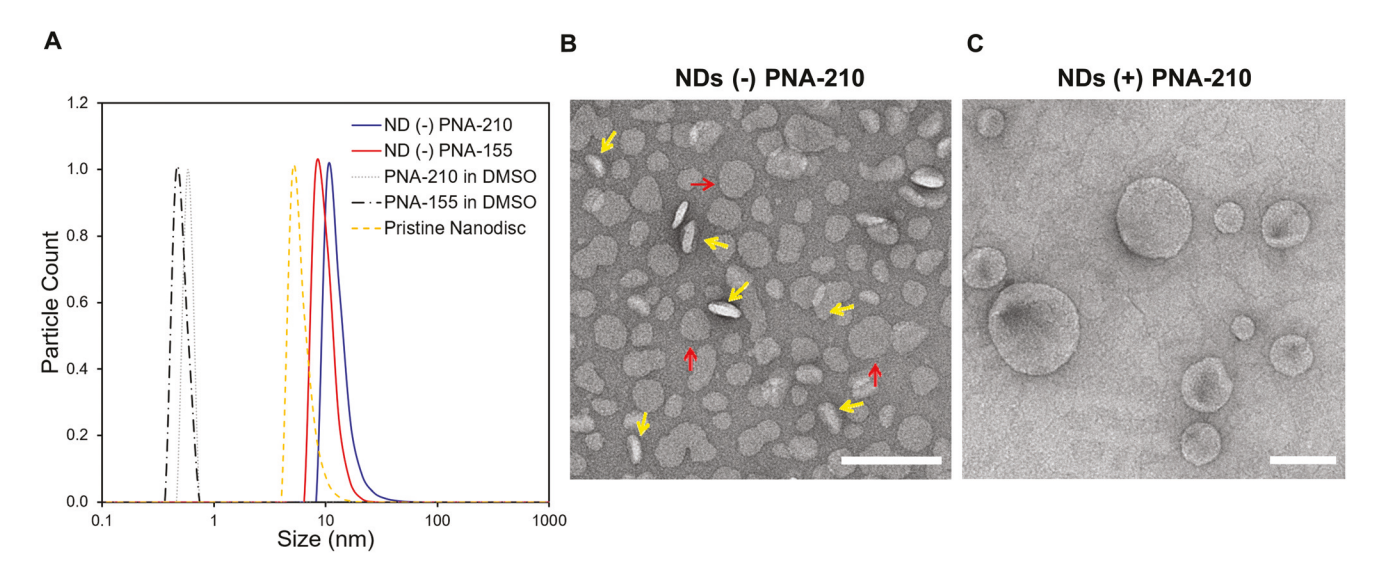


Fig. 1 (A) Size distribution of pristine nanodiscs (NDs), PNAs loaded NDs and free PNA dissolved in DMSO. The hydrodynamic radius  $R_{\rm H}$  of NPs was 10–12 nm for ND, consistent with the best fitting dimensions from SAXS data. (B and C) TEM images of negatively charged ND (–) and positively charged ND (+) containing a PNA: lipid molar ratio of 1: 2500. The planar and rim views are indicated by yellow and red arrows, respectively. The diameter of the NPs was ~30 nm for ND, consistent with the best fitting dimensions of SAXS and the hydrodynamic radius measured by DLS. Scale bars in all images are equal to 100 nm.

the positive charge of bicelles and the negative charge of PNA nucleobases interfered with the bicellar self-assembly.

Further, the morphologies of lipid/PNA complexes were examined by TEM and AFM. The TEM (Fig. 1B and Fig. S2 $\dagger$ ) and AFM images (Fig. S3 $\dagger$ ) indicate uniform discoidal morphology for both PNA-210 and PNA-155 (PNA: lipid = 1:2500), respectively, as encapsulated in the negatively charged bicelles. The fact that no noticeable difference in shape and size is found for both systems agrees well with the prior DLS results. Nevertheless, antimiR PNA-210 loaded in positively charged bicelles results in large vesicles (Fig. 1C), also consistent with the DLS data.

#### 3.3 Encapsulation efficiency

Incorporating hydrophobic small molecules into the lipid bilayer of liposomes or biomimetic membranes has been investigated experimentally<sup>39-42</sup> and theoretically.<sup>43-45</sup> The encapsulation efficiencies for hydrophobic molecules in liposomes are generally not high; 40,42 however, it has been reported that the bilayer defects induced by the short-chain lipids enhance the activity of the membrane to host lipophilic molecules. 46 It is expected that the encapsulation efficiency of hydrophobic molecules in bicelles is higher than in liposomes. Due to low solubility of PNAs in water, centrifugation is applied to the PNA-loaded bicelles to remove non-encapsulated PNA aggregates. In contrast to the colorless pristine bicelle solution, the PNA-loaded supernatants are pinkish depending on the concentration of encapsulated PNA. The entrapped amount of PNAs can be obtained from the UV-vis absorption spectra compared against a pre-calibrated UV-vis absorption spectrum, whose intensity is linearly dependent on the concentration of PNA (see Table S1 in ESI†).

The encapsulation efficiencies (EE) of antimiR PNA-210 and 155 encapsulated in bicelles are similar to each other at low PNA: lipid ratios (Fig. 2). However, with increased PNA: lipid ratio, the encapsulation efficiency decreased drastically (Fig. S4 $\dagger$ ). For instance, for a PNA: lipid ratio of 1:100, the EE is less than 10%, while with lower ratios and 1:2500, the EE in bicelles is 92 ± 7 (Fig. S4 and S5 $\dagger$ ). This further confirms that the lipophilicity of PNA allows for its interaction with the bicelle, thus forming a stable nanocomplex, and the excess insoluble PNA can be separated from the system through centrifugation. The fact that the centrifugation speed does not affect the experimental outcome of encapsulation efficiency, as suggested by Fig. S6, $\dagger$  indicates that the current centrifugation

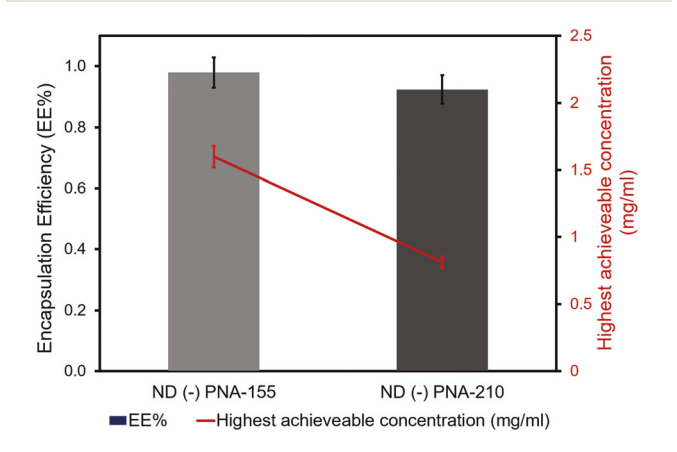


**Fig. 2** Encapsulation efficiencies (EE) of antimiR-155 and 210 PNAs in negatively charged NDs. The bar chart shows the EE, calculated ratio of encapsulated PNA molecules to the initial mass of PNA added. The line chart (right *y*-axis) indicates the highest achievable concentration of the PNAs encapsulated in NDs and stable in the aqueous phase.

speed and time are sufficient to separate the encapsulated and unencapsulated PNAs.

#### 3.4 Molecular modeling analysis of antimiR PNA sequences

The encapsulation mechanism of antimiR PNAs in bicelles can be understood through analysis of the molecular lipophilicity surface potential (MLSP) and the molecular electrostatic potential (MEP; Fig. 3) using VEGA ZZ software. The analysis shows that the TAMRA-labeled N-terminus of PNAs is more lipophilic and therefore can interact with the hydrophobic portion of the bicelles. However, the PNA backbone contains scattered hydrophilic domains, which could be exposed to the aqueous environment outside of the bicelles. The following SAXS analysis provides some insight into the location of PNA in the bicelles.

#### 3.5 SAXS analysis results

SAXS analysis allows structural characterizations through simulating the electron density distribution of formulated bicelles. SAXS measurements were performed on pristine, PNA-155-loaded, and PNA-210-loaded bicelles with different PNA: lipid ratios and surface charges, as shown in Fig. 4 (additional results are provided in the ESI Fig. S7, S8 and S9†). The lipid concentration of all samples is 1.0 wt%. In all the PNA-loaded bicelles, the general scatter feature contains a broad peak between q = 0.06 and  $0.20 \text{ Å}^{-1}$ , originated from the regular spacing between the phosphate headgroups of the two leaflets where the electron density is higher than that of the acyl chains. Therefore, the electron density profile across the bilayer (i.e., water - head group shell - hydrocarbon core head group shell - water) can be considered as a "square well". 21,47 The broad peak in all SAXS patterns suggests that the lipids maintain a bilayer structure.

A core-shell discoidal model (CSD model in ESI†) is employed to describe the bicelles, 21-23 where the core and shell represent the hydrophobic lipid tails and hydrophilic phosphate headgroups, respectively. The best fitting parameters used in the model for the SAXS data are listed in Table 1.  $R_{\rm core}$  and  $\rho_{\rm core}$  represent the radius and the electron density of the hydrophobic core, respectively, while  $t_{\text{shell}}$  and  $\rho_{\rm shell}$  are the thickness and electron density of phosphate shells along the normal of the bilayer, respectively. The rim has a thickness and electron density of  $t_{rim}$  and  $\rho_{rim}$ , respectively. The electron density of water,  $\rho_{\rm w}$ , is fixed throughout the fitting procedure. Moreover, we found the best fitting  $t_{\text{shell}}$  did not vary and thus was kept constant as well. The initial predictions of the electron densities used in the model were from the literature values for lipid bilayer nanoparticles elsewhere. 21,48 The CSD model can describe SAXS data well in q-range between 0.005 and 0.35  $\text{Å}^{-1}$ . SAXS data at higher q values involve detailed structures in the bilayer (e.g., the contrast between methylene and methyl groups) smaller than 1.8 nm, which is not considered in the current model. However, the SAXS data of bicelles (referred as to be "ND", representing nanodiscs) and PNA-loaded NDs seem to be similar. The comparison between the best fit of pristine ND and PNA-loaded SAXS data (individual plots at the bottom of Fig. 4) shows significant differences. The general conclusion of the best fitting procedure indicates that the encapsulation of antimiR-PNAs has no significant structural disturbance on the discoidal geometry, while some variation in the dimensions of the ND is found and will be discussed below.

The most drastic structural variation is the increase of total diameters for PNA-loaded NDs, changing from 244 Å to 300–400 Å, presumably caused by two factors: enlarged  $R_{\rm core}$  and  $t_{\rm rim}$ . The best fitting results show that  $R_{\rm core}$  has less than

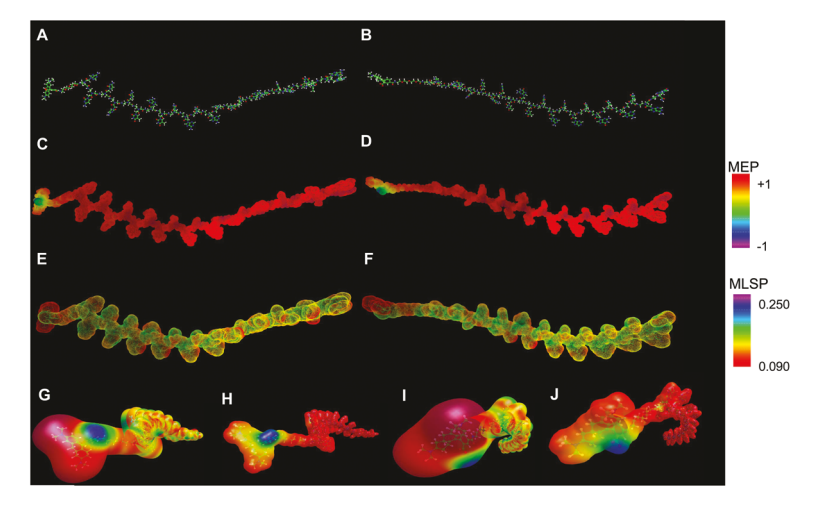


Fig. 3 Simulation studies for the antimiR PNA molecules using VEGA ZZ® software. (A and B) Chemical structure of antimiRs PNA-155 and PNA-210. TAMRA is at the far left side of the structure. (C and D) Molecular electrostatic potential (MEP) of PNA-155 and 210. (E and F) MLSP analysis of PNA-155 and PNA 210. Moving from blue to red on the scale indicates increasing MLSP. Red encircled portions show lipophilic regions exposed on the surface of the molecules, which provide an ideal segment in the molecule to be incorporated into the lipid bilayer. Both PNA molecules show low lipophilicity and low hydrophilicity in the main backbone, while the TAMRA portion is highly lipophilic. (G and I) A higher magnification of the TAMRA domains of antimiR PNA molecules is also provided in parts, (H and J) indicating the multiple hydrophilic and hydrophobic domains of the PNA backbone.

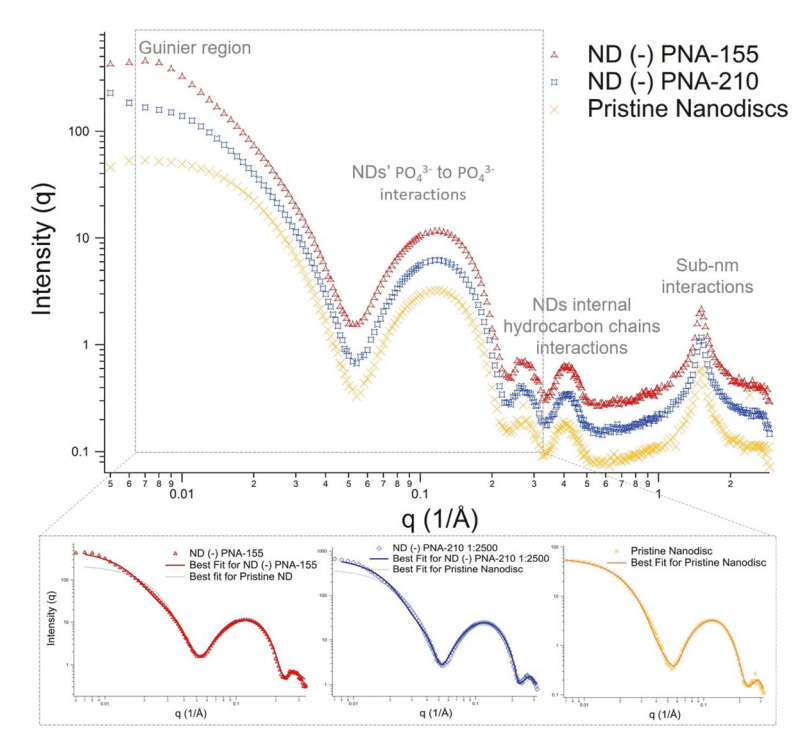


Fig. 4 SAXS results of antimiR-PNAs encapsulated in NDs. All the curves start with the Guinier region, which reciprocally correlates with the size of the nanocarriers. The broad peaks at  $0.07-0.2\ 1\ {\rm \AA}^{-1}$  belong to the headgroup distance of the phospholipid bilayers and bilayer thickness. Higher q peaks correlate with internal nanostructures of the NDs. Below, best fitting results are shown for each sample. As shown, to make a clear comparison, the results for the pristine NDs are also plotted *versus* the ND-PNA nanocomplexes.

Table 1 The best-fitting parameters obtained from the SAXS data of the NDs

	Core–shell discoidal model (with invariant $t_{\rm shell}$ = 14.9 Å, and $\rho_{\rm w}$ = 9.40 × 10 <sup>-6</sup> Å <sup>-2</sup> )						
	$ ho_{ m shell}$ , ×10 <sup>-6</sup> Å <sup>-2</sup>	$ ho_{ m rim}$ , ×10 <sup>-6</sup> Å <sup>-2</sup>	$t_{ m rim}$ , Å	$\rho_{\rm core}$ , ×10 <sup>-6</sup> Å <sup>-2</sup>	$t_{ m core}$ , Å	R <sub>core</sub> , Å	Disc diameter, Å
NDs ND(-) PNA-210 1 : 500 ND(-) PNA-210 1 : 2500 ND(-) PNA-155 1 : 2500	10.7(±0.1) 12.9(±0.9) 12.6(±0.4) 10.7(±1.7)	9.8(±0.1) 9.9(±0.6) 9.9(±1.5) 9.7(±3.5)	27.1(±0.5) 52.5(±4.5) 47.8(±2.9) 51.8(±2.8)	7.1(±1.1) 7.1(±2.2) 6.75(±1.2) 8.3(±0.8)	25.1(±0.2) 24.4(±0.3) 24.8(±0.7) 24.6(±0.6)	95(±8) 148(±11) 106(±1) 135(±2)	244(±9) 400(±16) 308(±4) 375(±5)

50% increase, while  $t_{rim}$  increases by more than 70%. Most interestingly, the best fitting shell ( $t_{\text{shell}}$ ) and core ( $t_{\text{core}}$ ) thicknesses are practically invariant. Further analysis on the best fitting  $t_{\text{rim}}$  (Fig. S8†) suggests that the range of  $t_{\text{rim}}$  has to be larger than 45 Å for all PNA-loaded NDs (50-55 Å for ND PNA 210 at 1:500; 45-51 Å for PNA 210 at 1:2500; and 48-55 for PNA 155 at 1:2500). The invariant bilayer thickness ( $2t_{\rm shell}$  +  $t_{\rm core}$ ) and significant increase of  $t_{\rm rim}$  suggest that the entrapped PNA molecules are mainly located at the rim of the ND. A reasonable explanation is that the hydrophobic portion of the PNA (the highly lipophilic TAMRA group) anchors into the bicelles' rim, resulting in the noticeable increase of rim thickness, while the planar bilayer of the discs remains unchanged from the pristine bicelles. This is consistent with the reported outcome of the interaction between inverse pluronic polymers and DHPC-containing vesicles. The DHPC-induced defects allow the polymers to anchor to the membrane at their hydrophobic region.46

#### 3.6 Cellular uptake studies

Further, cellular uptake of the formulated NDs was tested using TAMRA-conjugated PNA-155 and PNA-210 antimiRs. Flow cytometry analysis was performed to quantify cellular uptake. HeLa cells were treated with positively as well as negatively charged bicelles containing antimiR PNAs (PNA: lipid molar ratio of 1:2500) for 24 h, followed by flow cytometry analysis. We noticed the percentage of cells exhibiting fluorescence was significantly higher in the case of negatively charged bicelles (~95%) as compared to those positively charged (~43%, Fig. 5). This is most likely due to the morphological difference, i.e., small uniform discoidal bicelles (negatively charged) compared to a mixture of bicelles and vesicles (positively charged). In addition, the fluorescence signal was significantly higher in cells (higher cellular uptake) treated with negatively charged bicelles containing PNA-155-TAMRA as well as PNA-210-TAMRA (Fig. 5 and 6). No autofluor-

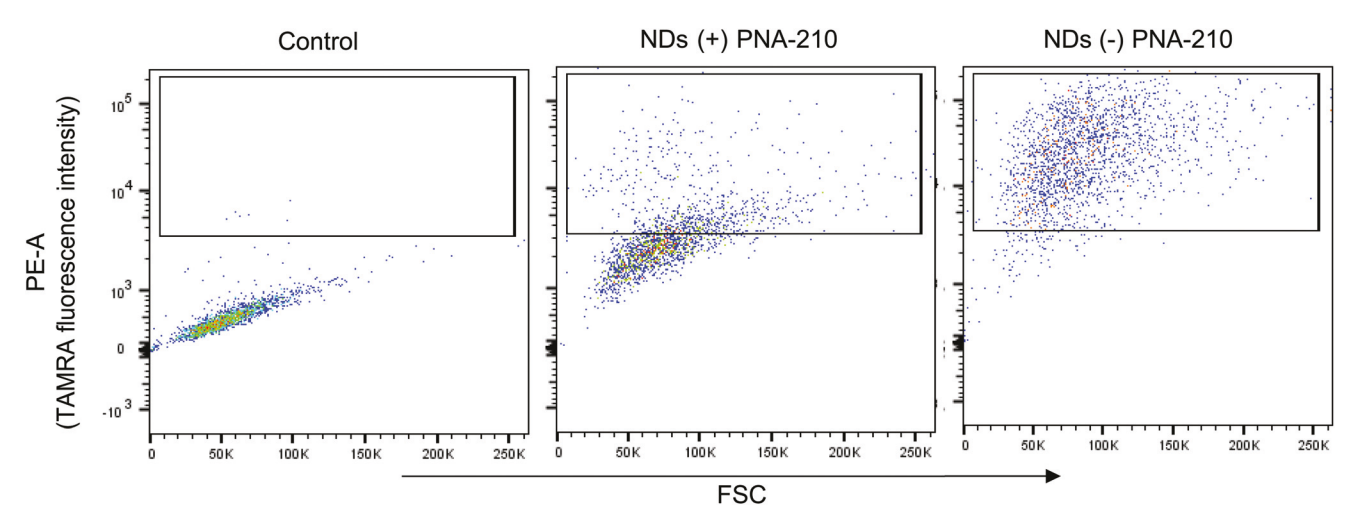


Fig. 5 FACS analysis of HeLa cells following incubation with the negative ND (–) and positive ND (+) containing PNA-210. 2000 cells were selected for the number of events.

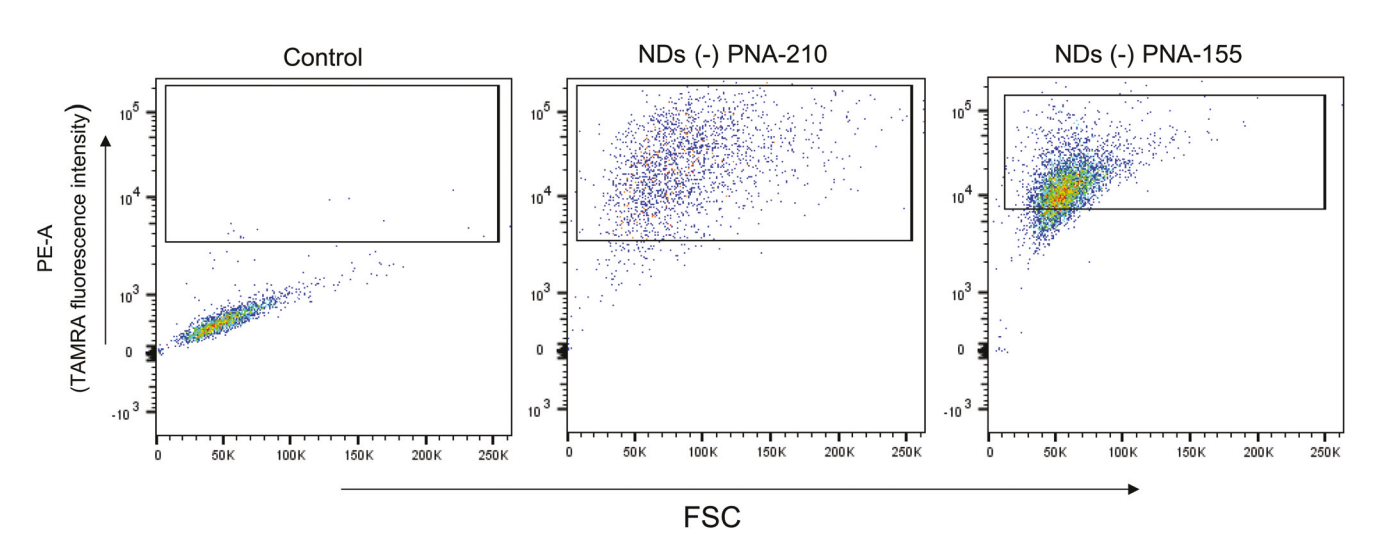


Fig. 6 FACS analysis of HeLa cells following incubation with the negative ND (–) containing PNA-210 and PNA-155. 5000 cells were selected for the number of events.

escence was observed in the untransfected cells in the TAMRA channel.

Next, cellular uptake of negatively charged bicelles containing PNA-155-TAMRA and PNA-210-TAMRA was confirmed using confocal microscopy. HeLa cells treated with PNA-155-TAMRA and PNA-210-TAMRA alone (same dose as present in the PNA-210 and PNA-155 bicelles) were used as control. HeLa cells in logarithmic phase were cultured in complete media and incubated with bicelles. After 24 h of incubation, cells were briefly washed three times with buffered saline and stained with nuclear dyes, followed by imaging. As shown in Fig. 7, bicelles containing PNA-155-TAMRA and PNA-210-TAMRA showed a narrow distribution of TAMRA signal in comparison to antimiR PNAs alone. Though we noticed significant distribution of PNA-TAMRA in the cytoplasm, we noted only a few puncta of TAMRA in the nuclei of cells treated with ND(-) con-

taining PNA-155-TAMRA. In parallel, cellular uptake analysis of PLGA nanoparticles containing antimiR PNA-155-TAMRA was also performed in HeLa cells. Bicelles showed not only a dramatic increase but also a more uniform uptake as compared to punctate distribution by PLGA NPs (Fig. S10†). Together, these results show that negatively charged bicelles contribute to the uniformity and high transfection efficiency of antimiR PNAs in the cells. In order to assess the toxicity of bicelles, we performed MTT assay in HEK293 primary cells. Minimal toxicity is noted as compared to the control samples (Fig. S11†). In addition, we also investigated the cellular uptake mechanism of negatively charged bicelles containing antimiR PNA-155-TAMRA.

#### 3.7 Mechanism of cellular uptake

We performed comprehensive studies to understand the cellular uptake mechanism of negatively charged bicelles contain-

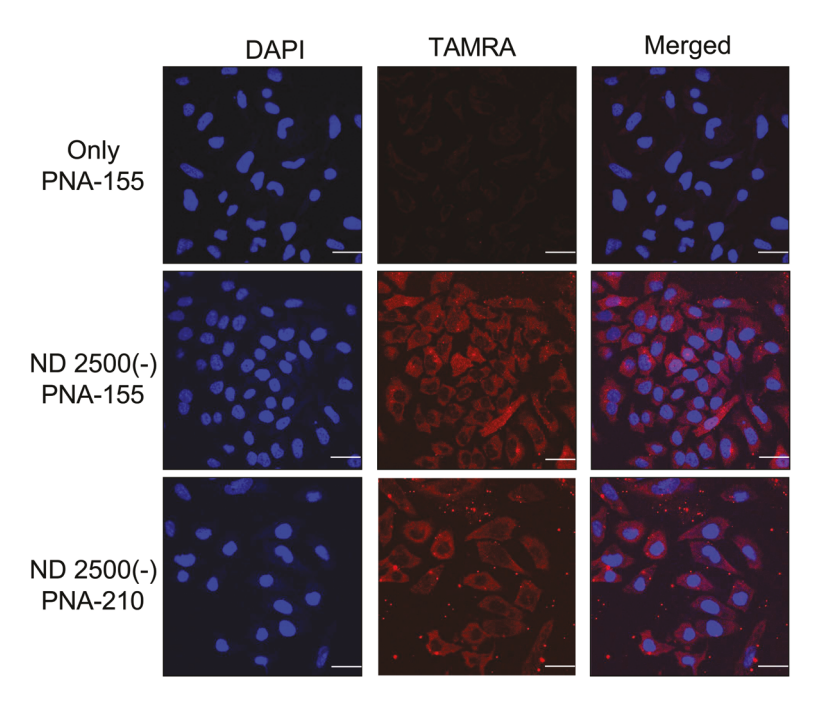


Fig. 7 Fluorescent images of HeLa cells incubated with negatively charged NDs for 24 h, followed by brief washing with PBS and incubation with DAPI (nuclear staining). Blue: nucleus (DAPI), red: PNA (TAMRA).

ing antimiR PNAs. First, we investigated whether endocytosis plays a significant role in the bicelles containing antimiR PNAs by performing temperature (37 °C  $\nu s$ . 4 °C)-dependent cellular uptake studies in HeLa cells. It has been proven that low temperature (4 °C) inhibits the endocytosis-based transport across the cell membrane. <sup>49</sup> Our confocal microscopy and flow cytometry results revealed that ND cellular uptake decreased significantly at 4 °C (Fig. S12†).

Further, three pharmacological inhibitors of the major endocytic pathway were used to study the cellular uptake mechanisms of negatively charged bicelles containing antimiR PNAs-155 in HeLa cells. Amiloride was used to inhibit membrane ruffling and macropinocytosis. 50 Chlorpromazine (CPZ) was employed to block clathrin-mediated endocytosis.<sup>51</sup> Genistein was used to inhibit clathrin-independent endocytosis or caveolae-mediated endocytosis.<sup>52</sup> Further, the inhibitors' concentrations were adjusted to achieve viability of HeLa cells (~95%) for 2 hours. Both flow cytometry analysis as well as confocal microscopy were used to evaluate the cellular uptake after treatment with inhibitors and bicelles. Our results indicate that negatively charged bicelles undergo cellular uptake by multiple endocytotic pathways. We noted that majority of the bicelles containing antimiR PNAs underwent endocytosis by caveolae-mediated endocytosis as well as macropinocytosis, followed by clathrin-mediated endocytosis (Fig. S13†).

#### 3.8 Quantification of antimiR activity of NDs in cell culture

Next, we investigated the antimiR-155 efficacy of formulated bicelles by quantitative RT-PCR analysis. For all experiments, cells treated with PNA-155 alone were used as control. We tested the expression of miR-155 in HeLa cell lines using

RT-PCR. HeLa cells exhibited overexpression of miR-155 and hence, we tested HeLa cell lines for comparing the efficacy of the formulated negatively charged bicelles containing PNA-155 at the PNA: lipid molar ratio of 1:2500. HeLa cells were treated with a sufficient amount of negatively charged bicelles to achieve a dose of 4  $\mu$ M PNA for 24 h. RNA was extracted and quantified by RT-PCR using U6 as a control. Unlike the control, PNA-155-TAMRA-loaded negatively charged bicelles reduced miR-155 expression by  $\sim\!\!50\%$  (Fig. 8). These results signify the antimiR activity of bicelles containing antimiR PNAs. Further, we also measured the antimiR-155 effect at

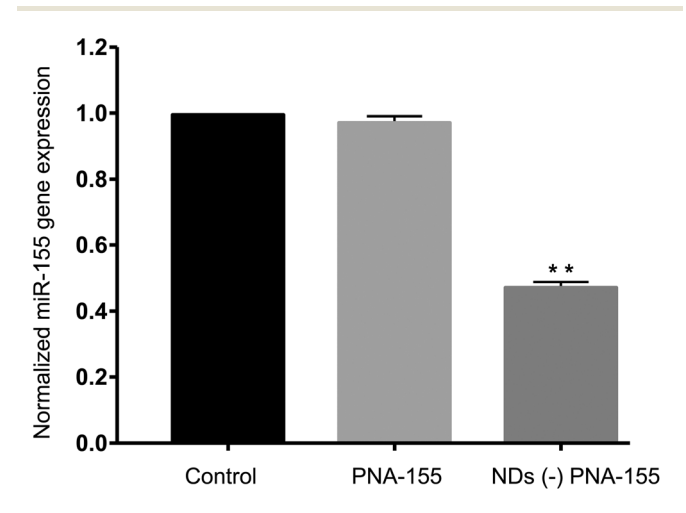


Fig. 8 miR-155 expression in HeLa cells after treatment with negatively charged NDs containing PNA-155. miR-155 expression relative to an average control (all normalized to U6, n = 3, \*p < 0.05).

protein levels using western blot analysis. p53 acts as a tumor suppressor and regulates cell division by inhibiting cells from growing and proliferating in an uncontrolled way. It has been established that miR-155 upregulation decreases the level of p53 protein. Our results revealed that pretreatment of HeLa cells with NDs containing PNA-155 led to  $\sim$ 39% upregulation of p53 (Fig. S14†).

# 4. Discussion

Despite the use of PNAs being first reported more than three decades ago, the cellular uptake of PNAs still circumscribes their broader clinical applications. In this work, using comprehensive structural and biophysical characterizations, fluorescence, as well as functional cell-based assay, we successfully demonstrated that lipid-based formulations can be used for the delivery of therapeutically active PNAs. It is noteworthy that the lipids (DPPG, DPPC and DHPC) used to constitute the bicelles are FDA-approved. We tested a series of positively and negatively charged NDs containing different PNA: lipid molar ratios. Our results indicate that negatively charged bicelles containing a 1:2500 molar ratio of PNA: lipid (the least disturbed composition) exhibit uniform size as well as discoidal shape. First, we confirmed that the 1:2500 ratio results in maximum encapsulation efficiency of two antimiRs, i.e., PNA-210 and PNA-155. Bicelles made of lipids with controlled size are attainable.<sup>23</sup> The PEGylated bicelles are very stable and only turn into vesicles of similar size through incubating at 55 °C or above for several hours, as confirmed by TEM, DLS, and SAXS.21 They have long-term stability in aqueous solutions and therefore are suitable as delivery carriers for drugs, vaccines, and genes for a variety of diseases.

The non-spherical geometries, such as rod-like and discoidal NPs, have been proven to permeate deeper into mammary tumors, greater than do their spherical counterparts with similar hydrodynamic sizes. 54,55 It has also been reported that NDs have high diffusion and penetration properties in collagen-rich environments.<sup>56</sup> Presumably, the small dimension along their thickness dimension promotes tumor penetration as compared with the symmetrically structured vesicles. Interestingly, recent mathematical modeling combined with in vitro and ex vivo experimentation demonstrated that discoidal geometries possessed the most favorable margination dynamics in the body.<sup>57</sup> Additionally, discoidal NPs show particular movement dynamics that favor the interaction with vessel walls more than spherical particles. 25,58 Though it has been demonstrated that positively charged NPs are internalized into the cell favorably due to their strong interaction with the negatively charged phospholipid components of the cell membrane,<sup>59</sup> their toxicity is also much higher. Hence, the negatively charged bicelles are also favorable in terms of safety as well as efficacy. 25 Our cell culture analysis did not show any noticeable toxicity.

Further, the morphology of PNA/bicelles was investigated using SAXS data analysis. The parameters of the core-shell

bicelle model, which best fits the SAXS data of bicelles, indicate axial shell thickness, radial shell thickness, core thickness, and radius consistent with literature values for pristine bicelles. 47 No significant difference was found in the SAXS patterns of PNA-loaded bicelles (i.e., discoidal shape with invariant bilayer thickness) compared to that of the pristine bicelle, except that the Guinier regime shifts to the lower q values, indicative of larger particles. The drastically increased rim thickness suggests that most of the entrapped PNAs are preferably localized at the rim region. The disc rim, mainly composed of short-chain DHPC, has a large spontaneous curvature and contains more defects, making it suitable to accommodate higher-curvature objects like large PNA ending domains. 60 Cell culture analysis substantiates that negatively charged bicelles show high transfection efficiency. We did not notice any punctated structures in the HeLa cells treated with bicelles, indicating that a good portion of bicelles may not undergo endosomal entrapment and thus uniformly distribute the antimiR PNAs in the cells. In addition, the fact that the negatively charged bicelles undergo cellular uptake by multiple endocytic mechanisms is also consistent with our previous report.<sup>20</sup>

# 5. Conclusions

In conclusion, our data demonstrate that PNAs can be efficiently delivered by negatively charged bicelles. This approach can be used to effectively reduce the levels of miRNA expression via an antisense mechanism. Improvements in accessibility to molecular targets and increased specificity could further be obtained by coating PNA-loaded bicelles with specific peptides, antibodies, and carbohydrate units. In summary, this work provides a novel platform for PNA delivery that can be developed for therapeutic purposes. The results presented in this report can serve as a promising platform based on PNA/ bicelle technology to control gene expression and regulation for diverse biomedical applications.

# Statistical analysis

Comparisons between two groups were carried out with Student's *t*-tests. Differences with *P* values of less than 0.05 were considered statistically significant.

#### Author contributions

M. P. N, R. B, A. T. R, and S. M designed the research; A. T. R, and S. M. performed the research; S. M and T. K. O performed the western blot analysis; M. P. N, R. B, A. T. R, and S. M analyzed the data and wrote the paper; L. Y. set up the SAXS experiment.

#### Conflicts of interest

The authors declare no competing financial interests.

# Acknowledgements

We thank Anisha Gupta for discussions and suggestions. This work was supported by University of Connecticut startup funds and the UConn START PPOC award (RB); A. T. R. is supported by NSF-CBET #1605971. The authors would like to acknowledge the beamtime of 16D-LiX at the NSLS-II (Brookhaven National Lab) through a beamtime proposal (BAG-302208). The LiX beamline is part of the Life Science Biomedical Technology Research resource, jointly supported by the National Institutes of Health, National Institute of General Medical Sciences, under Grant P41 GM111244, and by the Department of Energy Office of Biological and Environmental Research under Grant KP1605010, with additional support from NIH Grant S10 OD012331. NSLS-II is a U.S. Department of Energy (DOE) Office of Science User Facility, operated for the DOE Office of Science by Brookhaven National Laboratory under Contract No. DE-SC0012704. We also would like to thank Dr Jing Zhang and Dr George Lykotrafitis for their scientific support with the AFM analysis. Also we acknowledge Justin M. Fang for the technical help with TEM studies.

#### References

- 1 M. Egholm, *et al.*, PNA hybridizes to complementary oligonucleotides obeying the Watson-Crick hydrogen-bonding rules, *Nature*, 1993, **365**, 566–568, DOI: 10.1038/365566a0.
- 2 P. E. Nielsen, M. Egholm, R. H. Berg and O. Buchardt, Sequence-selective recognition of DNA by strand displacement with a thymine-substituted polyamide, *Science*, 1991, 254, 1497–1500, DOI: 10.1126/science.1962210.
- 3 P. E. Nielsen, Peptide nucleic acids: a new dimension to peptide libraries and aptamers, *Methods Enzymol.*, 1996, **267**, 426–433.
- 4 V. V. Demidov, *et al.*, Stability of peptide nucleic acids in human serum and cellular extracts, *Biochem. Pharmacol.*, 1994, **48**, 1310–1313.
- 5 A. Gupta, R. Bahal, M. Gupta, P. M. Glazer and W. M. Saltzman, Nanotechnology for delivery of peptide nucleic acids (PNAs), *J. Controlled Release*, 2016, 240, 302–311, DOI: 10.1016/j.jconrel.2016.01.005.
- 6 R. Bahal, N. A. McNeer, D. H. Ly, W. M. Saltzman and P. M. Glazer, Nanoparticle for delivery of antisense gammaPNA oligomers targeting CCR5, *Artif DNA PNA XNA*, 2013, 4, 49–57.
- 7 S. Malik, S. Oyaghire and R. Bahal, Applications of PNA-laden nanoparticles for hematological disorders, *Cell. Mol. Life Sci.*, 2019, **76**, 1057–1065, DOI: 10.1007/s00018-018-2979-5.
- 8 S. Malik, B. Asmara, Z. Moscato, J. K. Mukker and R. Bahal, Advances in Nanoparticle-based Delivery of Next Generation Peptide Nucleic Acids, *Curr. Pharm. Des.*, 2018, 43, 5164–5174, DOI: 10.2174/1381612825666190117164901.
- 9 J. P. Clarenc, G. Degols, J. P. Leonetti, P. Milhaud and B. Lebleu, Delivery of antisense oligonucleotides by poly(L-

- lysine) conjugation and liposome encapsulation, *Anticancer Drug Des.*, 1993, **8**, 81–94.
- 10 E. Delgado, *et al.*, beta-Catenin knockdown in liver tumor cells by a cell permeable gamma guanidine-based peptide nucleic acid, *Curr. Cancer Drug Targets*, 2013, **13**, 867–878.
- 11 B. Sahu, *et al.*, Synthesis of conformationally preorganized and cell-permeable guanidine-based gamma-peptide nucleic acids (gammaGPNAs), *J. Org. Chem.*, 2009, 74, 1509–1516, DOI: 10.1021/jo802211n.
- 12 C. Coester, J. Kreuter, H. von Briesen and K. Langer, Preparation of avidin-labelled gelatin nanoparticles as carriers for biotinylated peptide nucleic acid (PNA), *Int. J. Pharm.*, 2000, **196**, 147–149.
- 13 A. Bertucci, *et al.*, Intracellular delivery of peptide nucleic acid and organic molecules using zeolite-L nanocrystals, *Adv. Healthcare Mater.*, 2014, 3, 1812–1817, DOI: 10.1002/adhm.201400116.
- 14 A. Bertucci, *et al.*, Combined Delivery of Temozolomide and Anti-miR221 PNA Using Mesoporous Silica Nanoparticles Induces Apoptosis in Resistant Glioma Cells, *Small*, 2015, **11**, 5687–5695, DOI: 10.1002/smll.201500540.
- 15 K. Zhang, H. Fang, Z. Wang, J. S. Taylor and K. L. Wooley, Cationic shell-crosslinked knedel-like nanoparticles for highly efficient gene and oligonucleotide transfection of mammalian cells, *Biomaterials*, 2009, 30, 968–977, DOI: 10.1016/j.biomaterials.2008.10.057.
- 16 R. Bahal, *et al.*, In vivo correction of anaemia in beta-thalassemic mice by gammaPNA-mediated gene editing with nanoparticle delivery, *Nat. Commun.*, 2016, 7, 13304, DOI: 10.1038/ncomms13304.
- 17 A. S. Ricciardi, *et al.*, In utero nanoparticle delivery for site-specific genome editing, *Nat. Commun.*, 2018, **9**, 2481, DOI: 10.1038/s41467-018-04894-2.
- 18 U. Iqbal, *et al.*, Small unilamellar vesicles: a platform technology for molecular imaging of brain tumors, *Nanotechnology*, 2011, 22, 195102, DOI: 10.1088/0957-4484/22/19/195102.
- 19 M. P. Nieh, N. Kucerka and J. Katsaras, Spontaneously formed unilamellar vesicles, *Methods Enzymol.*, 2009, 465, 3–20, DOI: 10.1016/s0076-6879(09)65001-1.
- 20 E. Lyukmanova, et al., Lipid-protein nanodiscs for cell-free production of integral membrane proteins in a soluble and folded state: comparison with detergent micelles, bicelles and liposomes, *Biochim. Biophys. Acta, Biomembr.*, 2012, 1818, 349–358.
- 21 Y. Liu, M. Li, Y. Yang, Y. Xia and M.-P. Nieh, The effects of temperature, salinity, concentration and PEGylated lipid on the spontaneous nanostructures of bicellar mixtures, *Biochim. Biophys. Acta, Biomembr.*, 2014, **1838**, 1871–1880.
- 22 W. Aresh, *et al.*, The Morphology of Self-Assembled Lipid-Based Nanoparticles Affects Their Uptake by Cancer Cells, *J. Biomed. Nanotechnol.*, 2016, 12, 1852–1863.
- 23 Y. Liu, Y. Xia, A. T. Rad, W. Aresh and M.-P. Nieh, Stable Discoidal Bicelles: A Platform of Lipid Nanocarriers for Cellular Delivery, *Liposomes: Methods Protocols*, 2017, 273– 282.

- 24 S. Muro, *et al.*, Control of endothelial targeting and intracellular delivery of therapeutic enzymes by modulating the size and shape of ICAM-1-targeted carriers, *Mol. Ther.*, 2008, **16**, 1450–1458.
- 25 E. Blanco, H. Shen and M. Ferrari, Principles of nanoparticle design for overcoming biological barriers to drug delivery, *Nat. Biotechnol.*, 2015, 33, 941–951.
- 26 R. Agarwal, *et al.*, Mammalian cells preferentially internalize hydrogel nanodiscs over nanorods and use shape-specific uptake mechanisms, *Proc. Natl. Acad. Sci. U. S. A.*, 2013, **110**, 17247–17252.
- 27 J. Tan, S. Shah, A. Thomas, H. D. Ou-Yang and Y. Liu, The influence of size, shape and vessel geometry on nanoparticle distribution, *Microfluid. Nanofluid.*, 2013, 14, 77– 87.
- 28 L. Y. Chou, K. Ming and W. C. Chan, Strategies for the intracellular delivery of nanoparticles, *Chem. Soc. Rev.*, 2011, 40, 233–245.
- 29 R. Agarwal, *et al.*, Effect of shape, size, and aspect ratio on nanoparticle penetration and distribution inside solid tissues using 3D spheroid models, *Adv. Healthcare Mater.*, 2015, 4, 2269–2280.
- 30 J. DiFabio, *et al.*, in *AIP Conference Proceedings*, 030049, AIP Publishing.
- 31 L. Yang, Using an in-vacuum CCD detector for simultaneous small-and wide-angle scattering at beamline X9, *J. Synchrotron Radiat.*, 2013, **20**, 211–218.
- 32 P. Laad, G. Shete, S. R. Modi and A. K. Bansal, Differential surface properties of commercial crystalline telmisartan samples, *Eur. J. Pharm. Sci.*, 2013, **49**, 109–116.
- 33 B. Testa, P.-A. Carrupt, P. Gaillard, F. Billois and P. Weber, Lipophilicity in molecular modeling, *Pharm. Res.*, 1996, **13**,
- 34 E. Quijano, R. Bahal, A. Ricciardi, W. M. Saltzman and P. M. Glazer, Therapeutic Peptide Nucleic Acids: Principles, Limitations, and Opportunities, *Yale J. Biol. Med.*, 2017, **90**, 583–598.
- 35 L. Christensen, *et al.*, Solid-phase synthesis of peptide nucleic acids, *J. Pept. Sci.*, 1995, 1, 185–183, DOI: 10.1002/psc.310010304.
- 36 A. Gupta, *et al.*, Anti-tumor Activity of miniPEG-gamma-Modified PNAs to Inhibit MicroRNA-210 for Cancer Therapy, *Mol. Ther.-Nucleic Acids*, 2017, **9**, 111–119, DOI: 10.1016/j.omtn.2017.09.001.
- 37 I. A. Babar, *et al.*, Nanoparticle-based therapy in an in vivo microRNA-155 (miR-155)-dependent mouse model of lymphoma. Author summary, *Proc. Natl. Acad. Sci. U. S. A.*, 2012, **109**, 10140–10141, DOI: 10.1073/pnas.1201516109.
- 38 C. J. Cheng, *et al.*, MicroRNA silencing for cancer therapy targeted to the tumour microenvironment, *Nature*, 2015, **518**, 107–110, DOI: 10.1038/nature13905.
- 39 W. H. Binder, R. Sachsenhofer, D. Farnik and D. Blaas, Guiding the location of nanoparticles into vesicular structures: a morphological study, *Phys. Chem. Chem. Phys.*, 2007, **9**, 6435–6441.

40 M. R. Rasch, *et al.*, Hydrophobic gold nanoparticle self-assembly with phosphatidylcholine lipid: membrane-loaded and janus vesicles, *Nano Lett.*, 2010, **10**, 3733–3739.

- 41 G. Von White, Y. Chen, J. Roder-Hanna, G. D. Bothun and C. L. Kitchens, Structural and thermal analysis of lipid vesicles encapsulating hydrophobic gold nanoparticles, *ACS Nano*, 2012, **6**, 4678–4685.
- 42 X. An, F. Zhan and Y. Zhu, Smart photothermal-triggered bilayer phase transition in AuNPs-liposomes to release drug, *Langmuir*, 2013, 29, 1061–1068.
- 43 R. C. Van Lehn, *et al.*, Lipid tail protrusions mediate the insertion of nanoparticles into model cell membranes, *Nat. Commun.*, 2014, 5, 4482.
- 44 R. C. Van Lehn and A. Alexander-Katz, Fusion of ligand-coated nanoparticles with lipid bilayers: Effect of ligand flexibility, *J. Phys. Chem. A*, 2014, **118**, 5848–5856.
- 45 R. C. Van Lehn and A. Alexander-Katz, Pathway for insertion of amphiphilic nanoparticles into defect-free lipid bilayers from atomistic molecular dynamics simulations, *Soft Matter*, 2015, **11**, 3165–3175.
- 46 Y. Xia, *et al.*, Effects of Membrane Defects and Polymer Hydrophobicity on Networking Kinetics of Vesicles, *Langmuir*, 2017, 33, 5745–5751.
- 47 P.-W. Yang, T.-L. Lin, Y. Hu and U.-S. Jeng, Small-Angle X-ray Scattering studies on the structure of mixed DPPC/diC7PC micelles in aqueous solutions, *Chin. J. Phys.*, 2012, **50.** 349–356.
- 48 A. Albanese, P. S. Tang and W. C. Chan, The effect of nanoparticle size, shape, and surface chemistry on biological systems, *Annu. Rev. Biomed. Eng.*, 2012, **14**, 1–16.
- 49 E. Vives, P. Brodin and B. Lebleu, A truncated HIV-1 Tat protein basic domain rapidly translocates through the plasma membrane and accumulates in the cell nucleus, *J. Biol. Chem.*, 1997, 272, 16010–16017.
- 50 A. I. Ivanov, Pharmacological inhibition of endocytic pathways: is it specific enough to be useful?, *Methods Mol. Biol.*, 2008, **440**, 15–33, DOI: 10.1007/978-1-59745-178-9\_2.
- 51 J. Rejman, A. Bragonzi and M. Conese, Role of clathrinand caveolae-mediated endocytosis in gene transfer mediated by lipo- and polyplexes, *Mol. Ther.*, 2005, **12**, 468–474, DOI: 10.1016/j.ymthe.2005.03.038.
- 52 G. Sahay, D. Y. Alakhova and A. V. Kabanov, Endocytosis of nanomedicines, *J. Controlled Release*, 2010, **145**, 182–195, DOI: 10.1016/j.jconrel.2010.01.036.
- 53 K. Van Roosbroeck, *et al.*, Combining Anti-Mir-155 with Chemotherapy for the Treatment of Lung Cancers, *Clin. Cancer Res.*, 2017, 23, 2891–2904, DOI: 10.1158/1078-0432. CCR-16-1025.
- 54 V. P. Chauhan, *et al.*, Fluorescent nanorods and nanospheres for real-time in vivo probing of nanoparticle shape-dependent tumor penetration, *Angew. Chem., Int. Ed.*, 2011, **50**, 11417–11420, DOI: 10.1002/anie.201104449.
- 55 R. Agarwal, *et al.*, Mammalian cells preferentially internalize hydrogel nanodiscs over nanorods and use shape-specific uptake mechanisms, *Proc. Natl. Acad. Sci. U. S. A.*, 2013, **110**, 17247–17252, DOI: 10.1073/pnas.1305000110.

- 56 K. K. Ng, J. F. Lovell, A. Vedadi, T. Hajian and G. Zheng, Self-assembled porphyrin nanodiscs with structure-dependent activation for phototherapy and photodiagnostic applications, *ACS Nano*, 2013, 7, 3484–3490, DOI: 10.1021/nn400418y.
- 57 H. Lee, H. Fonge, B. Hoang, R. M. Reilly and C. Allen, The effects of particle size and molecular targeting on the intratumoral and subcellular distribution of polymeric nanoparticles, *Mol. Pharm.*, 2010, 7, 1195–1208.
- 58 F. Gentile, *et al.*, The effect of shape on the margination dynamics of non-neutrally buoyant particles in two-dimensional shear flows, *J. Biomech.*, 2008, **41**, 2312–2318.
- 59 A. Verma and F. Stellacci, Effect of surface properties on nanoparticle-cell interactions, *Small*, 2010, **6**, 12–21, DOI: 10.1002/smll.200901158.
- 60 H. Sharma and E. E. Dormidontova, Lipid Nanodisc-Templated Self-Assembly of Gold Nanoparticles into Strings and Rings, *ACS Nano*, 2017, **11**, 3651–3661.